Isolated Ni sites anchored on zeolites for direct synthesis of acetic acid from methane oxidative carbonylation

Jin Liu [a,b,1], Yao Wei [c,d,1], Ruitao Li [a,d], Yuxin Liu [a,b], Hailing Yu [a,d], Xuan Zhou [a,d], Bo Wu [a,e,*], Tiejun Lin [a,d,*], Liangshu Zhong [a,b,d,*]

[a] *CAS Key Laboratory of Low-Carbon Conversion Science and Engineering, Shanghai Advanced Research Institute, Chinese Academy of Sciences, Shanghai 201210, PR China*
[b] *School of Physical Science and Technology, ShanghaiTech University, Shanghai 201210, PR China*
[c] *Shanghai Institute of Applied Physics, Chinese Academy of Sciences, Shanghai 201800, PR China*
[d] *University of Chinese Academy of Sciences, Beijing 100049, PR China*
[e] *University of Science and Technology of China, Hefei, Anhui 230026, PR China*

ARTICLE INFO

ABSTRACT

Direct conversion of methane to acetic acid with high activity and selectivity over non-noble metal-based catalysts under mild reaction conditions remains a grand challenge. Specifically, 1.2Ni-ZSM-5 with 88.9 % isolated Ni sites achieved a high acetic acid yield of 2920 μmol/g$_{cat.}$ and a remarkable selectivity up to 82.3 % from methane oxidative carbonylation. Combined with high angle annular dark field scanning transmission electron microscopy, X-ray photoelectron spectroscopy, and X-ray absorption spectroscopy analyses, it was revealed that the isolated Ni species with Ni-O$_6$ moieties anchored in the micropores of ZSM-5 were suggested to be the active sites. The isotopic labeling experiments and monitoring of reaction intermediates demonstrated that CH$_3$COOH was formed via the direct coupling of methyl radicals and carbon monoxide molecules. This work suggests that the well-designed Ni sites can promote the transformation of CH$_4$ to C$_{2+}$ oxygenates instead of traditional C$_1$ oxygenates as main products.

1. Introduction

Methane (CH$_4$), a plentiful natural resource, [1] is a desirable feedstock for the production of value-added oxygenates such as methanol (CH$_3$OH), formic acid (HCOOH), ethanol (C$_2$H$_5$OH), and acetic acid (CH$_3$COOH) [2–4]. The selective transformation of CH$_4$ into CH$_3$COOH, [5] one of the significant essential intermediates, is more appealing and challenging than the production of C$_1$ oxygenates [6,7]. Nevertheless, the first C-H bond in CH$_4$ has a high bond dissociation energy, [8] making it challenging to selectively activate CH$_4$ without overoxidation [9–12]. Currently, the existing industrial procedures are accomplished indirectly through the initial formation of syngas, followed by the synthesis of methanol and the carbonylation of methanol [13–15]. Compared with the indirect route with an energy-intensive and polluting process, the production of CH$_3$COOH from CH$_4$ via one-step conversion could be more economical and promising, [4,16] despite

the difficulty of activating CH$_4$ and the ease of overoxidizing oxygenates [17].

Several active and selective catalysts have been explored for the oxidative transformation of CH$_4$ to value-added chemicals. Homogeneous catalysts such as RhCl$_3$, [18] Pd^{2+} in sulfuric acid, [19] and Mo catalysts, [20] exhibited excellent catalytic performance for the transformation of CH$_4$ towards CH$_3$COOH. However, in these catalytic processes, corrosive chemicals were used as the solvent and the catalyst recycling is difficult. Atomically dispersed metal catalysts have displayed intriguing reactivity and selectivity for methane oxidation due to their excellent atom utilization efficiency and distinct metal-support interaction [2]. For example, rhodium single atom catalysts with atomically dispersed metal sites such as isolated Rh$^+$ cation or Rh$_1$O$_5$ in ZSM-5 and Rh$_1$/pMOF have been reported for the oxidative carbonylation of methane to produce CH$_3$COOH [21–23]. In addition, the Fe binuclear sites and mononuclear Fe^{3+} species in ZSM-5 can also achieve

the production of CH_3COOH from the methane oxidative carbonylation at a low temperature of 50 °C [24,25].

Despite showing satisfactory catalytic performance over these catalysts, it is desirable to achieve high activity and high selectivity towards methane conversion to acetic acid with non-noble catalysts under mild conditions. Ni single atoms embedded in porous carbon nitride were synthesized for the transformation of CH_4 to C_1 oxygenates by generating methyl radicals ($\cdot CH_3$) in the presence of H_2O_2 [26]. Based on these findings, we believe that Ni atoms are a promising candidate for efficient conversion of methane to oxygenates. However, the traditional Ni-based catalysts typically produce C_1 products such as methanol as the main product and the generation of C_2 products such as acetic acid has not been achieved [27–29].

ZSM-5 as a famous zeolite with well-defined porous, which can provide a specific coordination site for anchoring isolated atom sites such as iron and copper, imitating natural enzymatic systems. The adjustable acidities of ZSM-5 enable the favorable formation of CH_3COOH via CO insertion after CH_4 activation [21,22,30]. In the present work, we chose H-ZSM-5 as a support to anchor Ni atoms for methane conversion to oxygenates. In the previous study, Fe-BN/ZSM-5 exhibited an acetic acid yield of 1540 $\mu mol/g_{cat.}$ and CH_3COOH selectivity of 60 % in oxygenated product under 5 bar of CO and 25 bar of CH_4, with 654 μmol of H_2O_2 at 50 °C for 10 h. However, the catalytic activity was limited due to the low density of active sites and the formation of over-oxidizing oxygenates. Herein, we reported a reactive Ni-ZSM-5 catalyst with isolated nickel sites anchored in zeolites for oxidative transformation of CH_4 in the presence of CO and hydro-peroxide as oxidant at 50 °C. A high yield of acetic acid (2920 $\mu mol/g_{cat.}$) with a selectivity of 82.3 % in oxygenated products was obtained over the 1.2Ni-ZSM-5 catalyst. Through isotopically labeled experiments and the monitoring of reaction intermediates, it can be determined that the formation of CH_3COOH originates directly from the coupling between CH_4 and CO.

2. Experimental

2.1. Catalyst preparation

Commercial ZSM-5 (Nankai Chemicals) was calcined at 550 °C for 3 hours under static air before impregnation. The incipient impregnation method was used to prepare the Ni-ZSM-5 catalyst. Typically, a certain Ni precursor, $NiCl_2 \cdot 6H_2O$ (Aladdin), is doped to the calcined ZSM-5 powder with continuous stirring. After impregnation, the samples were dried in an oven at 80 °C overnight and calcined at 400 °C for 4 h in the air. The amount of the Ni precursor was varied to obtain various Ni mass loadings. These catalysts were named 0.2Ni-ZSM-5, 1.2Ni-ZSM-5, 2.0Ni-ZSM-5, and 2.8Ni-ZSM-5, respectively. For comparison, Ni-ZSM-5-IE was synthesized using the ion exchange method. The 10 g of H-ZSM-5 was added to the prepared Ni solution (0.1 M, 150 mL), followed by vigorous stirring at 80 °C for 2 h. After the ion-exchange step, the products were washed with deionized water several times. The obtained solid was dried and calcined under the same conditions.

2.2. Catalyst characterization

Transmission electron microscopy (TEM) images and high-resolution TEM (HRTEM) images were obtained on a JEOL JEM-2011 system operating voltage at 100 kV. The aberration-corrected high-angle annular dark field scanning transmission electron microscope (AC-HAADF-STEM) was performed on FEI Titan Themis with an accelerating voltage of 300 KV. The samples for electron microscopy characterization were prepared by directly dropping in ethanol solvent on cubic grid coated holey carbon film.

X-ray diffraction (XRD) measurements were recorded on a Rigaku Ultima IV X-ray instrument with Cu K_α ($\lambda = 1.54056$ Å) radiation with a beam voltage of 40 kV and current of 40 mA, and the scanning speed was 2°/min. The mass loadings of Ni in Ni-ZSM-5 catalysts were determined by inductively coupled plasma optical emission spectrometry (ICP-OES, Agilent ICP-OES 5110), in which all the samples (~100 mg) are completely dissolved in the HF solution.

N_2 adsorption and desorption isothermal curves were obtained on an ASAP 2420 system apparatus (Micromeritics Instruments, USA) to measure the Brunauer-Emmett-Teller (BET) specific surface area, and all of the samples were degassed at 200 °C for 6 h before tests.

X-ray photoelectron spectroscopy (XPS) was performed to examine the chemical state of surface elements in Ni-ZSM-5 catalysts by an ESCLAB250 spectrometer, using a monochromatic Al Kα radiation source ($hv = 1486.6$ eV). The binding energies were calibrated using the C1s peak at 284.8 eV as a reference.

X-ray absorption fine structure (XAFS) spectroscopy at Ni K-edge was conducted on the BL11B beamline at the Shanghai Synchrotron Radiation Facility (SSRF), operated at 3.5 GeV with injection currents of 210 mA, to investigate the structure feature and the coordination environment of the Ni-ZSM-5 samples. A Si (111) double-crystal monochromator was used to reduce the harmonic component of the monochrome beam, and Ni foil was used as a reference sample. The obtained XAFS data were processed to obtain the normalized X-ray absorption near edge structure (XANES) and extended X-ray absorption fine structure (EXAFS) spectra using the Athena software. Corresponding fitting curves of EXAFS spectra were processed by the Artemis module in the IFEFFIT packages.

The electron paramagnetic resonance (EPR) spectra were recorded on a Bruker A300 spectrophotometer equipped with a liquid nitrogen cryostat, and 5,5-dimethyl-1-pyrroline-N-oxide (DMPO) was used as the radical scavenger to detect the generated radical species during the CH_4 interaction with H_2O_2. The radicals are represented by species with the "·" symbol in the prefix. For example, the hydroxyl and methyl radicals are denoted by "·OH" and "·CH_3" respectively.

The in-situ CO diffuse reflectance infrared Fourier transform (DRIFTS) spectra were tested on a Thermo-Fisher Nicolet iS10 instrument equipped with the liquid nitrogen-cooled mercury cadmium telluride (MCT) detector. All of the samples were pretreated at 150 °C with 20 mL/min of Ar gas to remove water and impurities adsorbed on the catalyst surface, and then the background spectrum was collected. After being cooled down to 50 °C, the gas flow containing CH_4, CO, and H_2O_2 was purged for 30 min to collect the spectra through 64 scans at a resolution of 4 cm^{-1} in the wavenumber range of 4000–650 cm^{-1}. Authors are expected to mind the margins diligently. Conference papers need to be stamped with conference data and paginated for inclusion in the proceedings. If your manuscript bleeds into margins, you will be required to resubmit and delay the proceedings preparation in the process.

2.3. Evaluation of catalytic performance

The catalytic performance of the selective oxidation of methane to acetic acid was evaluated using a 50 mL batch reactor (Shanghai Yanzheng Experimental Instrument Co., Ltd.). Typically, 20 mg of catalyst, 20 mL of deionized water, and 50 μL (0.654 mmol) of H_2O_2 (30 wt %, Adamas-beta®) were added to the autoclave. Then, the autoclave was purged with 5 bars of 97 % CO/N_2 three times and charged with a mixture of 97 % CO/N_2 and 95 % CH_4/Ar at a total pressure of 30 bars at room temperature. The reaction temperature was then increased to 50 °C while stirring the reaction mixture at 1000 rpm.

2.4. Analysis of products

The gaseous phase products were analyzed by a thermal conductivity detector (TCD) and FID with a mechanized unit. The oxygenates (HCOOH, CH_3OOH, CH_3OH, and CH_3COOH) were analyzed using Bruker AVANCE III 600 M ^{1}H NMR and ^{13}C NMR spectra. To quantify

these products, standard curves were established by correlating the ratio of the peak area of oxygenated products to the peak area of sodium 4,4-Dimethyl-4-silapentane-1-sulfonate (DSS), and the quantity of oxygenates. The integrated areas of CH_3OH ($\delta = 3.35$ ppm), CH_3OOH ($\delta = 3.85$ ppm), $HCOOH$ ($\delta = 8.35$ ppm), and CH_3COOH ($\delta = 2.07$ ppm) were calculated by setting the peak area of the standard DSS at $\delta = 0$ ppm. The product yield (μmol/$g_{cat.}$), specific yield based on per gram Ni (mmol/g_{Ni}), selectivity of oxygenates (%), and selectivity of CH_3COOH in oxygenated products (%, CO_2-Free), conversion of H_2O_2 (%) and gain factor (defined as mol of oxygenated produced/mol of H_2O_2 consumed) were calculated as follows Eqs. (1)–(6):

$$\text{Product yield}\ (\mu\text{mol} \big/ g_{cat.}) = \frac{n_{products}}{g_{cat.}} \tag{1}$$

$$\text{Specific yield}\ (\text{mmol} \big/ g_{Ni}) = \frac{n_{products}}{g_{Ni}} \tag{2}$$

$$\text{Oxygenates selectivity}(\%) = \frac{n_{(oxygenate\ products)}}{n_{(total\ products)}} \times 100\% \tag{3}$$

$$CH_3COOH\ \text{selectivity}(\%) = \frac{n_{CH_3COOH}}{n_{(oxygenate\ products)}} \times 100\% \tag{4}$$

$$\text{Conversion of}\ H_2O_2\ (\%) = \frac{n_{(H_2O_2)consumed}}{n_{(H_2O_2)in}} \times 100\% \tag{5}$$

$$\text{Gain factor (G)} = \frac{n_{(oxygenate\ products)}}{n_{(H_2O_2)consumed}} \tag{6}$$

Isotopic Labeling Experiments. The autoclave was charged with $^{13}CH_4$, CO, and H_2O_2, or CH_4, ^{13}CO, and H_2O_2 for the desired reaction time at 50 °C. 500 μL of obtained liquor sample, 100 μL of D_2O, and 100 μL of DSS were added into the NMR Tube. The signals of $^{13}CH_3COOH$ and $CH_3^{13}COOH$ are located at 21 and 177.1 ppm, respectively.

3. Results and discussion

3.1. Structure characterization of Ni-ZSM-5

A series of Ni-ZSM-5 catalysts with varying Ni content were synthesized using an impregnation method [31]. The actual Ni mass loading in Ni-ZSM-5 samples was determined by inductively coupled plasma optical emission spectrometry (ICP-OES) and listed in Table S1. In the high-resolution transmission electron microscopy (HR)TEM image of the 2.8Ni-ZSM-5 sample (Figure S1), NiO nanoparticles can be observed on the surface of the ZSM-5. In contrast, in the (HR)TEM image of the 1.2Ni-ZSM-5 sample (Figure S2), NiO nanoparticles were not observed, which suggests the possibility of Ni species dispersing in the internal pore of Ni [28]. Aberration-corrected high-angle annular dark field scanning transmission electron microscopy (AC-HAADF-STEM) was performed to observe the morphology structure of the 1.2Ni-ZSM-5 sample and investigate the dispersion and forms of Ni species. From Fig. 1a and b, it can be observed that the ZSM-5 support in the 1.2Ni-ZSM-5 catalyst appeared as prismatic structures with dimensions around 1 μm. In the higher magnification AC-HAADF-STEM images (Fig. 1c, and e (local magnification in Fig. 1d indicated by the red dashed box)), the white bright spots uniformly distributed on the pore structures of the ZSM-5 support can be observed, which are speculated to be dispersed Ni atoms. Furthermore, the obtained EDS image (Fig. 1f) shows that Si, Al, and Ni were uniformly dispersed on the ZSM-5
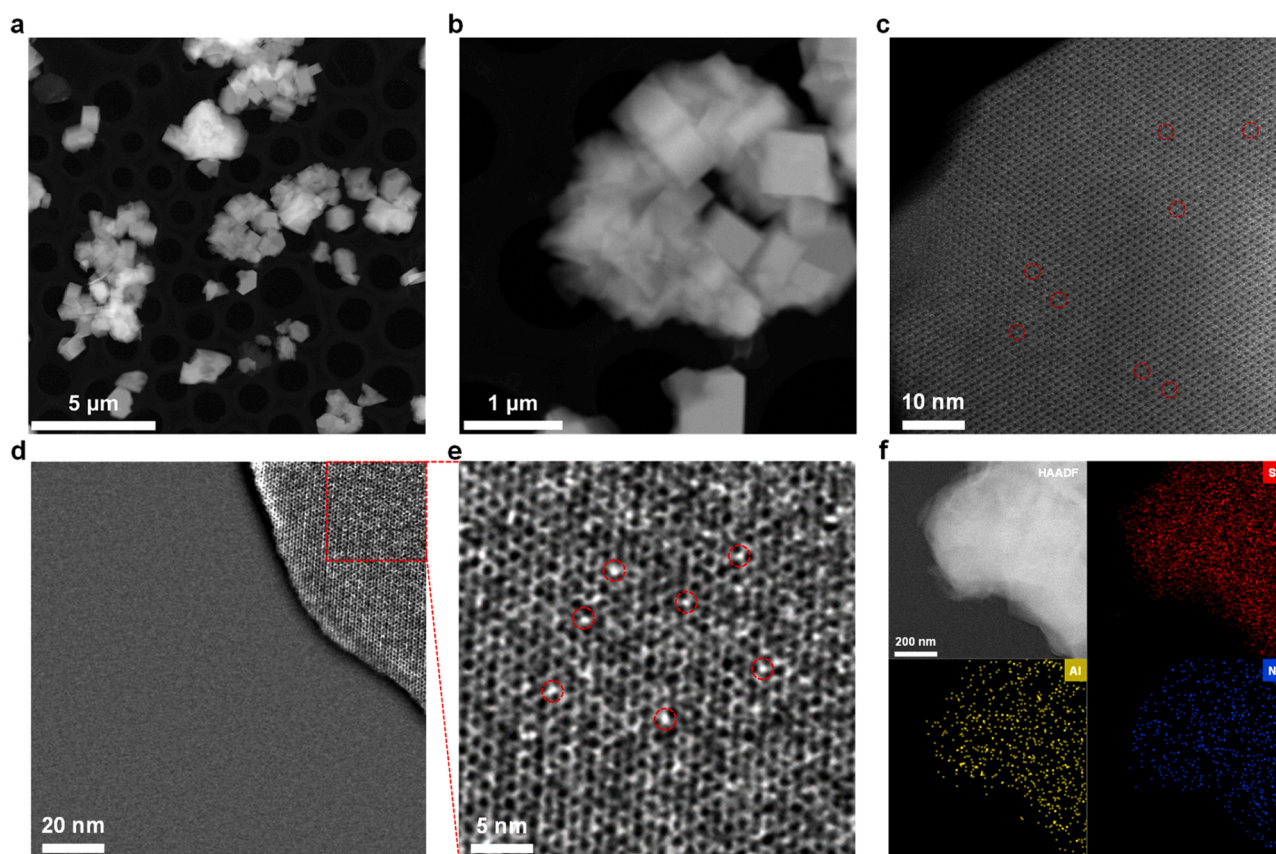

Fig. 1. The structural characterization for Ni-ZSM-5. (a-b) TEM images and (c-e) HAADF-STEM images for 1.2Ni-ZSM-5. The atomically dispersed Ni species were cycled by red spots in panels c and e. (f) HAADF-STEM image and the corresponding EDX elemental mapping for the distribution of Si, Al, and Ni elements for 1.2Ni-ZSM-5.

support.

The crystalline phase and pore structure characteristics of the Ni-ZSM-5 catalyst samples were characterized by X-ray diffraction (XRD) and Nitrogen adsorption/desorption analysis, respectively. Fig. 2a shows the XRD patterns of the samples, and Figure S3 presents the nitrogen sorption isotherms. The structural properties of various samples are listed in Table S2. In the XRD patterns (Fig. 2a) of catalysts with higher Ni loading, such as 2.0Ni-ZSM-5 and 2.8Ni-ZSM-5, a diffraction peak appeared at 43.3°, which can be assigned to the diffraction signal of the (200) crystal plane of NiO, [32] indicating the presence of NiO nanoparticles on the external pore surface of the ZSM-5. However, in the XRD patterns of the catalysts with lower Ni loading, such as 0.2Ni-ZSM-5 and 1.2Ni-ZSM-5 (Fig. 2a), no diffraction signal belonging to the NiO phase was observed, indicating that Ni species highly dispersed when the loadings lower than 1.2 wt %. Furthermore, the XRD patterns of all samples maintained the diffraction signals corresponding to the crystalline structure of the ZSM-5 support, indicating that the impregnation and subsequent calcination processes did not cause any structural changes to the ZSM-5 support. The characteristics of Type-I isotherms at relative pressures of $0 < P/P_0 < 0.4$ and a hysteresis loop of Type H1 at $P/P_0 = 0.45–0.99$ were exhibited in the Nitrogen sorption isotherms of the Ni-ZSM-5 samples (Figure S3), indicating the presence of a micropore structure similar to that of the zeolite ZSM-5 [33]. This suggests that the preparation process did not alter the pore structure characteristics of the support. According to the structural properties of the Ni-ZSM-5 samples (Table S2), the surface area and pore volume of the samples did not show significant changes compared with ZSM-5 at lower Ni loadings. However, further increase in Ni loading led to a decrease in the surface area and pore volume of the zeolite, which was speculated to be caused by the formation of more NiO nanoparticles on the zeolite support [34].

3.2. Chemical state and coordination structure of Ni species in Ni-ZSM-5

The chemical valence states of Ni species in Ni-ZSM-5 samples were characterized by X-ray photoelectron spectroscopy (XPS) measurements, and the XPS spectra in Ni $2p_{3/2}$ region of Ni-ZSM-5 with different Ni contents are shown in Figure S4. To verify the presence of Ni species within the zeolite framework, the samples were subjected to Ar$^+$ sputtering treatment before XPS testing, and the XPS spectra of 1.2Ni-ZSM-5 before and after sputtering treatment are shown in Fig. 2b. According to previous literature, major peaks at 854.0 eV, 855.5 eV, and a broad
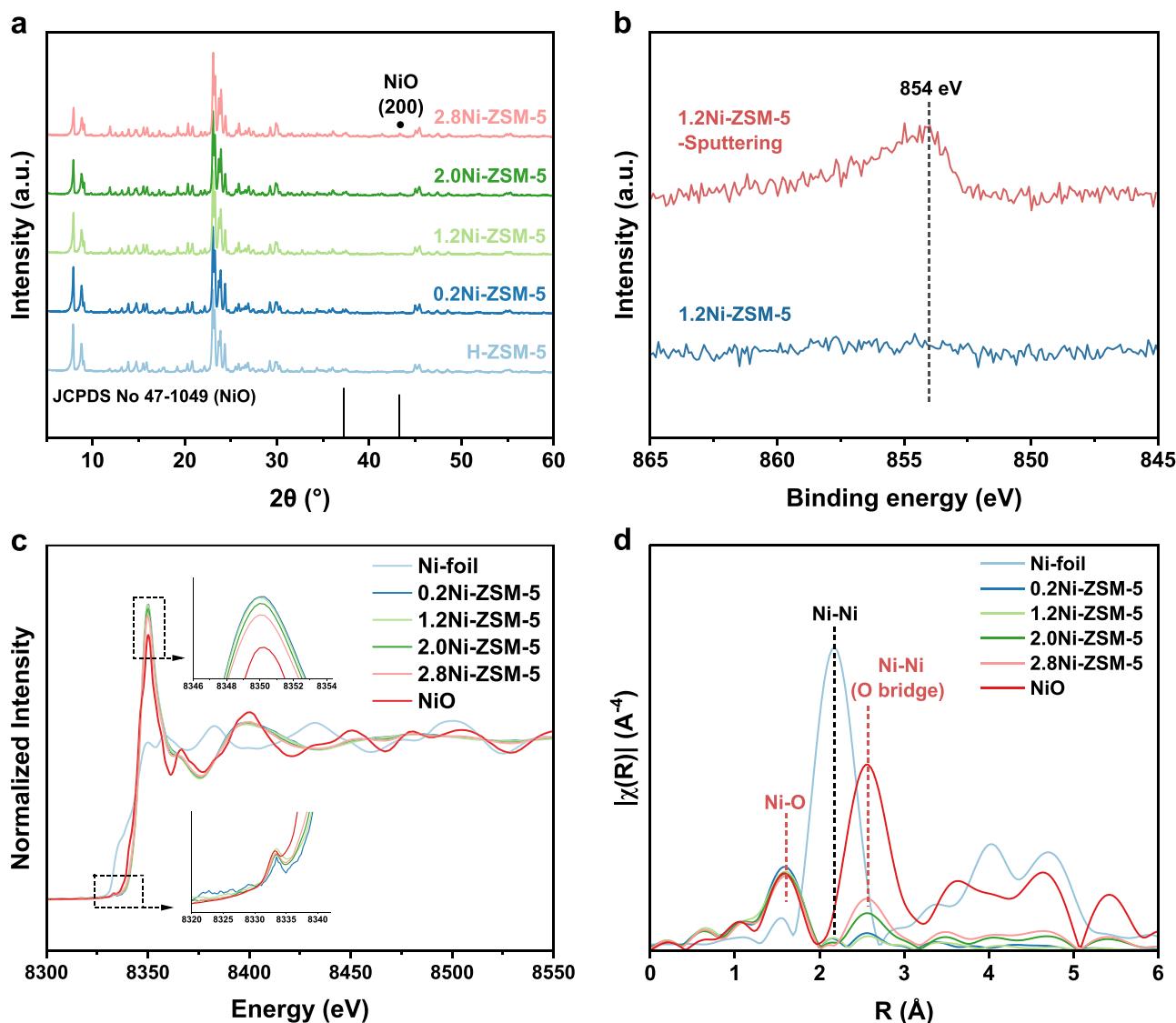

Fig. 2. The spectroscopic characterization for Ni-ZSM-5. (a) X-ray diffraction patterns of Ni-ZSM-5 samples and pristine ZSM-5. (b) The Ni $2p_{3/2}$ photoemission spectra of as-synthesized 1.2Ni-ZSM-5 before and after Ar$^+$ ion sputtering. (c) Normalized Ni K-edge XANES spectra of Ni-ZSM-5, NiO, and standard Ni foil. (d) k^3-weighted Ni K-edge EXAFS spectra of Ni-ZSM-5, NiO and standard Ni foil.

signal peak at 861.0 eV were included in the NiO photoemission spectrum [32,35,36]. In the XPS spectra of the samples with higher Ni contents, such as 2.0Ni-ZSM-5 and 2.8Ni-ZSM-5, several peaks at 854.5 eV, 856.3 eV, and 862.0 eV can be observed, combining with the observation of larger NiO particles from TEM and HRTEM images (Fig. S1), we can conclude that larger NiO merely existed on the external surface of the ZSM-5 matrix [32,36]. Due to the interaction between Ni species and the zeolite support, these peaks exhibit higher binding energies than the characteristic signal peaks of NiO [37]. However, in the samples with lower Ni loading, such as 0.2Ni-ZSM-5 and 1.2Ni-ZSM-5, there is no obvious photoemission signal of Ni species, indicating that the amount of NiO particles in these samples is minimal and difficult to be detected, which is also consistent with the as-obtained XRD results. Nevertheless, the peak at 854.5 eV is observed after the Ar^+ sputtering treatment for the 1.2Ni-ZSM-5 catalyst (Fig. 2b). This suggests that the Ni species inside the zeolite pores were detected after removing the surface silicon layer through Ar^+ sputtering treatment. In other words, for the samples with lower loading, the Ni species are mainly located inside the zeolite pores [21]. According to previous studies of the Tao's group, the peaks at 853.8 eV, 856.0 eV, and 861.0 eV corresponded to the electron transitions of photoexcited Ni atoms from the 3d orbitals to the ligand electron states ($3d^9L^{-1}$, $3d^9LL_{far}^{-1}$, and $3d^{10}L^{-2}$) from near to far distances [32,36,38]. In the Ni $2p_{3/2}$ spectrum after sputtering treatment, only a peak at 854.0 eV was observed, which could be attributed to Ni^{2+}, while the peak at 856.0 eV and 861.0 eV were absent. This Ni species was interpreted as bent mono (μ-oxo) dinickel anchored on the internal pore of zeolite [28]. Similar Ni species signals can be observed in our experimental results, suggesting the presence of Ni^{2+} species anchored on the internal pore of zeolite.

The chemical state and coordination environment of Ni species in the Ni-ZSM-5 sample were further characterized through X-ray absorption spectroscopy (XAS) measurement. The Ni K-edge X-ray absorption near-edge structure (XANES) of the Ni-ZSM-5 catalyst (Fig. 2c) shows the absorption edge energy of Ni-ZSM-5 was closer to that of NiO, [34,39] indicating that the Ni species in Ni-ZSM-5 are predominantly in the divalent form and coordinated with the O atoms [40]. The white line (~8350 eV) originates from 1s-4p transmission. As the metal loading increases, the white line peak gradually shifts towards the NiO reference, indicating a subsequent increase in the content of NiO nanoparticles similar to the NiO reference. For all samples, a sharp peak is observed in the pre-edge range (~8334 eV), which is associated with a 1s-3d photoelectron transition and is sensitive to the local geometry of Ni sites [41,42]. Here, both single Ni site and NiO nanoparticles possess similar NiO_6 local structural moiety. This octahedral geometry can generate weak electric quadrupole transmission, which is the main contribution of pre-edge. Additionally, it was observed that the absorption edge energy of the sample with lower Ni loading exhibited higher energy (approximately 2 eV) [43]. This could be attributed to the interaction between the Ni species and the zeolite support. As the Ni content increased, the energy of the K-edge absorption edge of Ni species slightly decreased and approached that of the reference NiO sample [34].

The Fourier-transformed k^3-weighted EXAFS spectra of Ni K-edge for Ni-ZSM-5 samples in the R-space were shown in Fig. 2d, and the corresponding fitting data was listed in Table S3 (FT-EXAFS fitting results in Figure S5). For the 0.2Ni-ZSM-5 catalyst sample, the average bond length of Ni-O was determined to be 2.05 Å, corresponding to a coordination number of 6.3. Additionally, there existed Ni-Ni contribution from the Ni-O-Ni bridges, which was characterized by an average bond length of 2.93 Å and a coordination number of 0.7. As the Ni content increased, the coordination number of the second shell Ni-O-Ni gradually increased. The mainly second distant coordination shells around Ni cations are similar to the characteristics of crystalline NiO, and the intensity of these coordination shells increases with the higher Ni loading [34,39]. This indicated that the increased Ni content led to the formation of more NiO on the zeolite. This observation is also consistent with

the results of XRD spectra (Fig. 2a) and XPS spectra (Figure S4). It is worth noting that, despite the low Ni content in the 0.2Ni-ZSM-5 sample, a small amount of Ni-O-Ni coordination is still present.

In order to obtain samples without Ni-O-Ni coordination for comparison, Ni-ZSM-5-IE was synthesized using the ion-exchange method. The FT-EXAFS fitting results of the as-obtained sample only showed the presence of the first shell Ni-O coordination at 2.04 Å. Principal component analysis (PCA) was performed on the XANES spectra of Ni-ZSM-5-IE and crystalline NiO [44]. The linear combination of these two different components sufficiently described the XANES spectra of each sample. Linear Combination Fit (LCF) analysis was used to describe the XANES spectra of Ni-ZSM-5 samples with different Ni contents by linearly combining the spectra of NiO and Ni-ZSM-5-IE (Figure S6). The Ni-ZSM-5-IE component represented Ni-O coordination, which corresponded to isolated Ni^{2+} anchored in the internal pore of the zeolite. The NiO component represented Ni-O-Ni coordination, which referred to the formation of NiO nanoparticles on the zeolite support. The relative contents of these two Ni species are listed in Table S4. The fitting results indicated that with an increase in the loading amount of Ni, the proportion of NiO nanoparticles in the sample increases, while the proportion of isolated Ni^{2+} anchored in the internal pore of the zeolite decreases. This result was consistent with the FT-EXAFS fitting results (Figure S5), exhibiting a stronger signal of the second shell Ni-O-Ni coordination in samples with higher Ni loading [34]. Furthermore, it suggested that an increase in the Ni loading inevitably led to a higher abundance of NiO nanoparticles formed on the external surface of ZSM-5 as observed in HRTEM characterization of 2.8Ni-ZSM-5 (Figure S2).

3.3. Catalytic activity and selectivity of Ni-ZSM-5 for synthesis of acetic acid from methane

The catalytic performance of various Ni-ZSM-5 samples was investigated with H_2O_2 as the oxidant and CH_4 and CO coexisted. After the reaction, the products in the aqueous phase were detected using quantitative nuclear magnetic resonance (NMR) analysis. After 10 hours of reaction at 50 °C, compared with the ZSM-5, a significant amount of liquid phase products was formed with the introduction of Ni. From Fig. 3a, it can be observed that with increasing Ni loading, the formation of liquid phase products, primarily acetic acid (CH_3COOH), increased. The highest oxygenated product yield of 4956 $\mu mol/g_{cat.}$ and a selectivity of 82.3 % towards CH_3COOH (2920 $\mu mol/g_{cat.}$) were achieved on the 1.2Ni-ZSM-5 catalyst, which is comparable to these noble metal-based catalysts (Table S5). The impact of H_2O_2 concentration and catalyst amount was investigateded over 1.2Ni-ZSM-5 (Figure S7), where higher H_2O_2 concentration leads to increased product amount but decreased acetic acid selectivity. Additionally, increasing the catalyst dosage further enhances the product content without significant changes in product selectivity. However, further increase in Ni loading led to a decrease in catalytic activity, with the catalytic performance of the 2.8Ni-ZSM-5 catalyst dropping to less than half of that of the 1.2Ni-ZSM-5 sample. At low Ni mass loadings (≤1.2 wt %), the catalytic activity increased with the increased NiO_6 sites. Conversely, at high Ni mass loadings (≥2.0 wt %), the high proportion of NiO particles impeded the activation of H_2O_2 to highly active species, leading to a lower catalytic activity toward methane oxidative carbonylation (Figure S8). Combining with the characterization results of the catalyst, it was found that higher Ni loading resulted in the formation of more NiO nanoparticles, [28,40] which is speculated to be the reason for the decrease in catalytic performance. Consequently, the elevated abundance of NiO nanoparticles on the catalyst surface should induce a decline in both the reaction activity and product selectivity.

To accurately calculate the specific yield based on per mole Ni sites, the catalytic activity of ZSM-5 was subtracted. Figure S9 presented the catalytic activity on the Ni sites in the Ni-ZSM-5 catalyst. The catalytic activity on the isolated Ni sites in both Ni-ZSM-5-IE (303 mmol/g_{Ni}) and
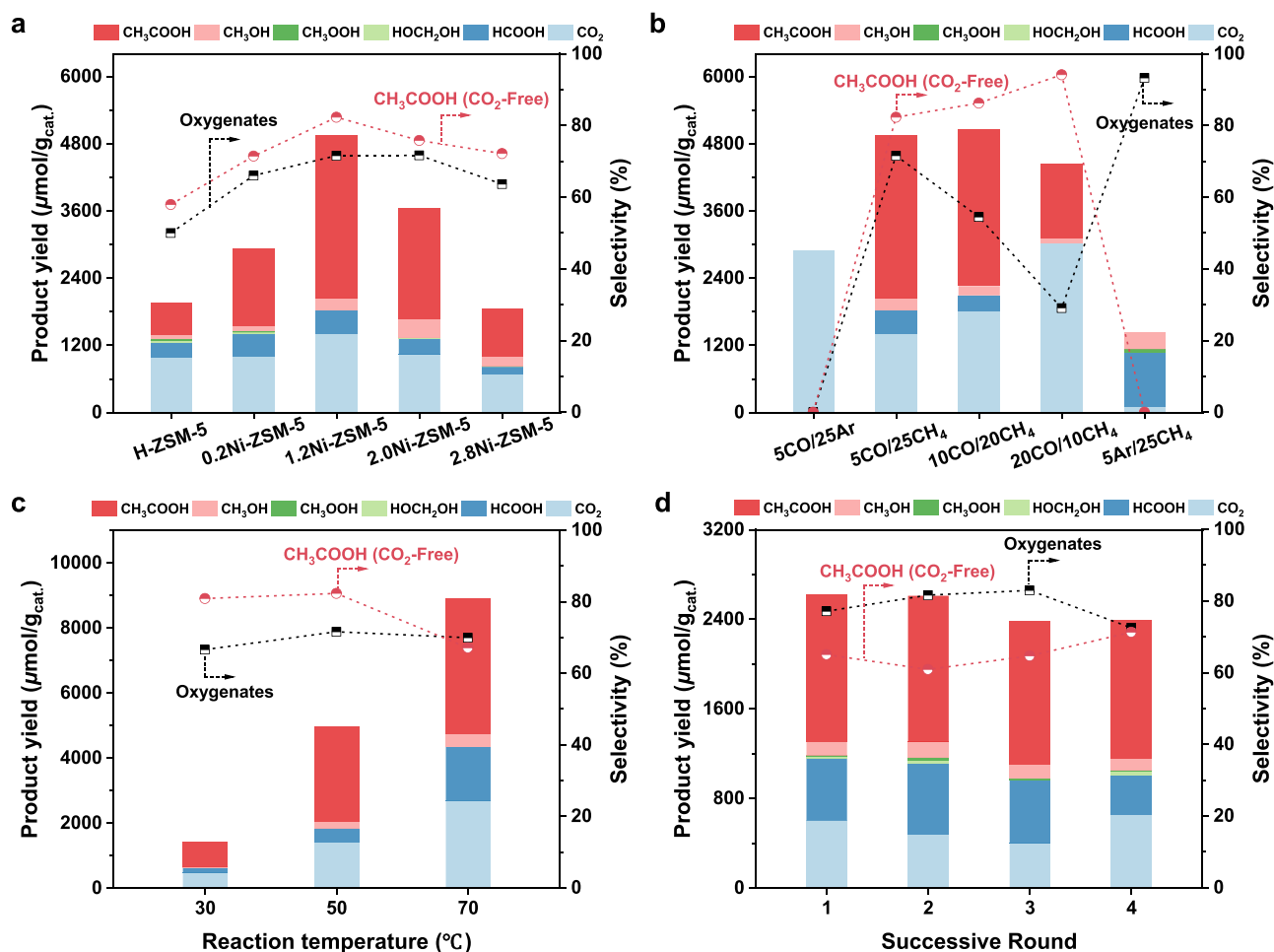
Fig. 3. Product yield and oxygenates selectivity for selective oxidation of CH_4 with CO and H_2O_2. (a) Effect of Ni loadings on CH_4 oxidation over Ni-ZSM-5. (b) Effect of CO/CH_4 ratio on CH_4 oxidation over 1.2Ni-ZSM-5. (c) Effect of reaction temperature on CH_4 oxidation over 1.2Ni-ZSM-5. (d) Stability test of 1.2Ni-ZSM-5. Reaction conditions: (a) 5 bar of CO and 25 bar of CH_4, 654 μmol of H_2O_2, 20 mL of H_2O, reaction time: 10 h, 50 °C, catalyst amount: 20 mg; (b) 654 μmol of H_2O_2, 20 mL of H_2O, reaction time: 10 h, 50 °C, catalyst amount: 20 mg; (c) 5 bar of CO and 25 bar of CH_4, 654 μmol of H_2O_2, 20 mL of H_2O, reaction time: 10 h, catalyst amount: 20 mg; (d) 5 bar of CO and 25 bar of CH_4, 1300 μmol of H_2O_2, 20 mL of H_2O, reaction time: 3 h, 50 °C, catalyst amount: 40 mg.

1.2Ni-ZSM-5 (286 mmol/g_{Ni}) is comparable but lower than that of 0.2Ni-ZSM-5 (543 mmol/g_{Ni}). It is speculated that the increased number of Ni sites in Ni-ZSM-5-IE and 1.2Ni-ZSM-5 reduces the utilization efficiency of Ni site [30]. As a result, 0.2Ni-ZSM-5 exhibits a higher specific yield based on per weight Ni. Additionally, since Ni-ZSM-5-IE does not contain NiO NPs, it exhibits higher selectivity towards oxygenate products. Both 0.2Ni-ZSM-5 and 1.2Ni-ZSM-5 have similar proportions of NiO NPs and exhibit similar but lower selectivity towards oxygenate products. On the other hand, 1.2Ni-ZSM-5 achieves higher acetic acid selectivity due to a higher content of Ni sites, as Ni sites serve as favorable active centers for acetic acid production, despite a decrease in the efficiency of Ni site utilization.

In order to confirm whether Ni-O-Ni is the key specie that contributes to the conversion of methane to acetic acid, we prepared NiO-ZSM-5 by calcinating a mixture of NiO and ZSM-5. The weight loading of Ni in NiO-ZSM-5 is same as that of 1.2Ni-ZSM-5. XRD analysis (Figure S10) showed that a diffraction peak located at 43.3° was observed, indicating that the formation of NiO species (PDF# 47–1049) [32,45]. We then tested the catalytic performance toward methane oxidation under 5 bar of CO and 25 bar of CH_4 with 654 μmol of H_2O_2 at 50 °C for 3 h (Figure S11). The result showed that NiO-ZSM-5 presented a low CH_3COOH yield of 364 μmol/$g_{cat.}$ and selectivity of 66.7 %, which was similar to pure ZSM-5 (283 μmol/$g_{cat.}$ and 81.9 %). However, there was significant increase in the CO_2 amount compared with pure ZSM-5, indicated that NiO would lead to the production of CO_2 and did not

serve as the key species contributing to the formation of acetic acid.

The effect of CO partial pressure was further investigated (Fig. 3b). When 5 bar CO was charged as the feed gas with a total pressure of 30 bar, CO_2 was the major product. When CH_4 gas was co-introduced (5 bar of CO and 25 bar of CH_4), the oxygenated products accounted for 71.6 %, and CH_3COOH was detected as the main product in the liquid phase. When the feed gas included 25 bar of CH_4 and 5 bar of Ar as balance gas, a high selectivity of 93.3 % for oxygenated products was achieved. However, the main product in the liquid phase was HCOOH, indicating that the introduction of CO gas favors the formation of CH_3COOH. Furthermore, after the introduction of CO, in the presence of both CO and CH_4, the product yield increased from 1788 μmol/$g_{cat.}$ to 4956 μmol/$g_{cat.}$, indicating that the introduction of CO can promote the activation of H_2O_2 and CH_4.[25,46]. When the CH_4/CO ratio was increased from 5/25–20/10, a higher CH_3COOH selectivity in oxygenate products was acquired and increased from 82.3 % to 94.2 %. In addition, the yield of C1 oxygenate products was decreased with the increase of CO partial pressure, suggested that the higher CO partial pressure was not beneficial for the production of C1 oxygenates such as HCOOH. It indicated that higher CO partial pressure is advantageous for the CH_3COOH selectivity and CH_3COOH products keep stable in liquid products. A comparable CH_3COOH yield of 2799 μmol/$g_{cat.}$ and higher CH_3COOH selectivity of 86.2 % was achieved at $10CO/20CH_4$ compared with $5CO/25CH_4$.

The effect of reaction temperature on the catalytic performance was

also investigated as shown in Fig. 3c. It was observed that higher reaction temperature was advantageous for the methane oxidation reaction. When the reaction temperature reached 70 °C, a product yield of 8905 μmol/g$_{cat.}$ was acquired for the 1.2Ni-ZSM-5 catalyst. Among them, 4178 μmol/g$_{cat.}$ constituted the target product CH$_3$COOH, with an acetic acid selectivity of 67.1%. This suggests that even at elevated temperature, which could potentially lead to the over-oxidation of products to CO$_2$ or HCOOH, a relatively high selectivity towards acetic acid could still be maintained. The time-dependent reaction progress analysis exhibited in Figure S12 revealed a gradual increase in the product yield over time, while maintaining a CH$_3$COOH selectivity range of 78.4–90.0 % for these oxygenated products.

To evaluate the catalyst stability, the spent catalyst was filtered and washed with deionized water, and the dried catalyst was further used for subsequent cycles under the same conditions. The catalytic performance after four cycles of react ion was shown in Fig. 3d. It can be observed that the catalyst after the catalytic reaction still maintained its original catalytic activity, and the product yield and selectivity remained almost unchanged after four reaction cycles. In addition, no obvious change for crystalline structure, chemical state and coordinated environment can be found for the spent 1.2Ni-ZSM-5 (1.2Ni-ZSM-5-used), according to

the XRD, XPS, and XAS results (Figure S13). It suggests a high stability of 1.2Ni-ZSM-5 catalyst for methane conversion.

Other transition metals-based SACs were prepared including 1.2Cu-ZSM-5 and 1.2Co-ZSM-5 via similar synthesis steps to that of 1.2Ni-ZSM-5, and were used for CH$_4$ oxidative carbonylation at the same reaction conditions. As shown in Figure S14, CH$_3$OH as main oxygenate product was obtained over 1.2Cu-ZSM-5, despite the notable product yield. Though CH$_3$COOH selectivity of ~80 % in oxygenate product was achieved, low product yield and low oxygenates selectivity observed over 1.2Co-ZSM-5. Therefore, the transition metal Ni supported on ZSM-5 catalyst is more advantageous than other transition metals for the CH$_3$COOH synthesis from CH$_4$ methane oxidative carbonylation.

3.4. Catalytic mechanism exploration and discussion

In order to obtain molecular-level evidence regarding the direct involvement of CO in the synthesis of CH$_3$COOH, isotopic labeling experiments were conducted over the 1.2Ni-ZSM-5 catalyst. When ^{13}CH$_4$ was used as a reactant, the chemical shifts (δ) at 20.7 ppm in the ^{13}C NMR spectrum (Fig. 4a) and at 2.17 and 1.95 ppm in the ^{1}H NMR spectrum (Fig. 4b) can be detected, which were attributed to the
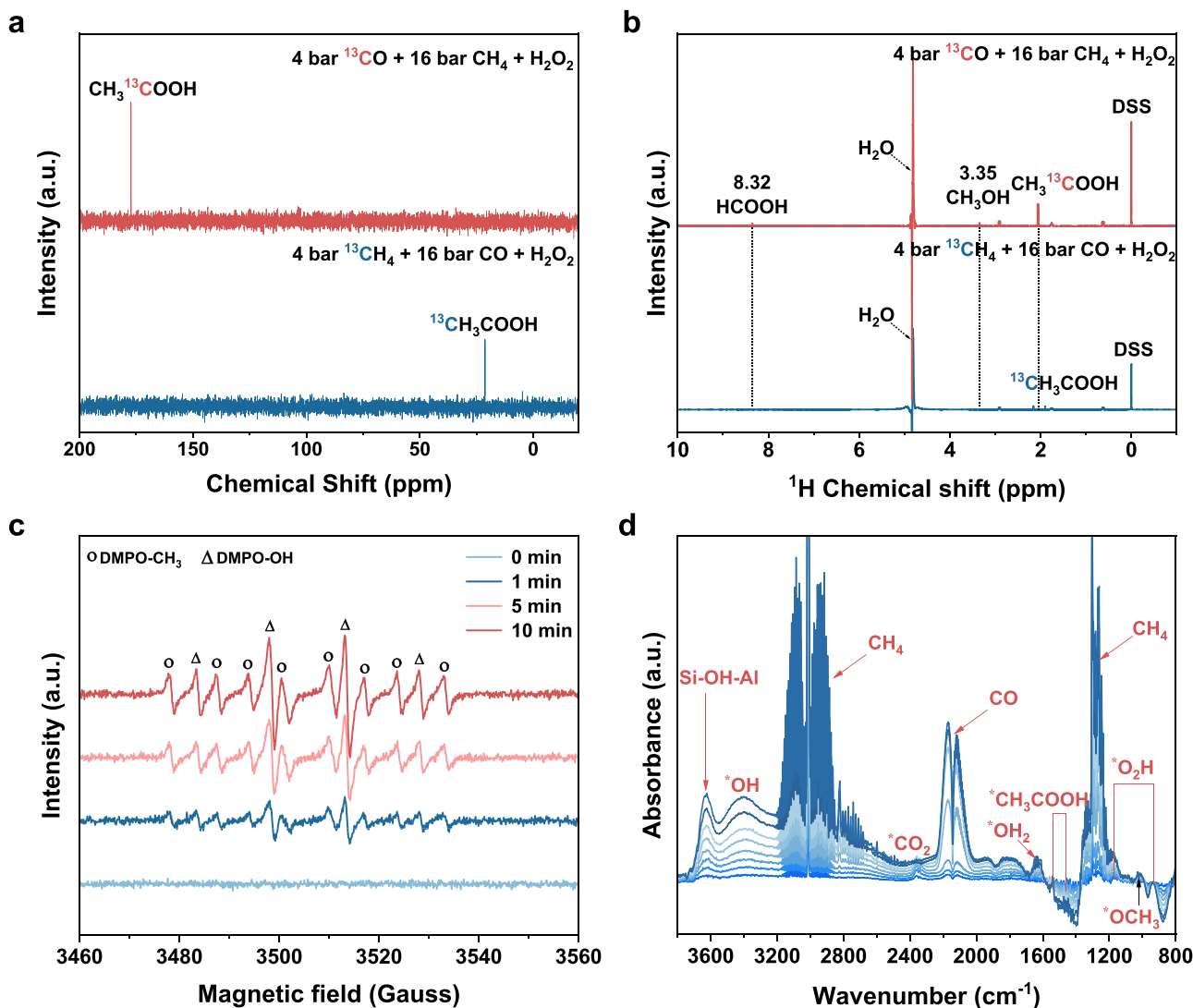

Fig. 4. Catalytic mechanism for the production of acetic acid. (a) ^{13}C NMR spectrum and (b) ^{1}H NMR spectrum of isotopic labeling experiments over 1.2Ni-ZSM-5. (c) EPR spectra and (d) *In-situ* DRIFTS spectra for 1.2Ni-ZSM-5. Reaction conditions: (a) and (b) 4 bar of ^{13}CH$_4$ and 16 bar of CO, or 4 bar of ^{13}CO and 16 bar of CH$_4$, 1300 μmol of H$_2$O$_2$, 20 mL of H$_2$O, 50 °C, reaction time: 10 h, catalyst amount: 20 mg; (c) CH$_4$ and H$_2$O$_2$ as the reactants with DMPO as a trapping agent; (d) CH$_4$, CO, H$_2$O$_2$ and water vapor as the reactants, 50 °C.

presence of $^{13}CH_3COOH$. In comparison, when ^{13}CO was used as a reactant, the chemical shift at 177.1 ppm in the ^{13}C NMR spectrum (Fig. 4**a**) and satellite peaks at 2.06 and 2.07 ppm in the ^1H NMR spectrum (Fig. 4**b**) can be observed, corresponding to $CH_3{}^{13}COOH$. Based on the above findings, we can deduce that CH_3COOH is entirely derived from the direct carbon-carbon coupling reaction between CH_4 and CO [47]. In order to definitively eliminate the possibility of CH_3COOH formation through the conversion of CH_3OH and HCOOH, control experiments were performed utilizing $CH_3OH+CO+H_2O_2$ and $HCOOH+CO+H_2O_2$ as reactants. The results presented in Table S6 demonstrate the absence of CH_3COOH in these reactions, thereby providing conclusive evidence that supports our initial assumption.

Electron paramagnetic resonance (EPR) spectroscopy was employed using the radical trap 5,5-Dimethyl-1-pyrroline-N-oxide (DMPO) to detect and identify various radical species. As depicted in Fig. 4**c**, distinct signals corresponding to ·OH and ·CH_3 were observed in the presence of CH_4 and H_2O_2 [48]. It suggested that H_2O_2 can activate the C-H bond of CH_4 over 1.2Ni-ZSM-5 catalyst, leading to the formation of ·CH_3 radicals [49,50]. Furthermore, the *in situ* diffuse reflectance-infrared Fourier-transform spectroscopy (DRIFTS) was performed to characterize the CH_4 oxidation reaction intermediates over 1.2Ni-ZSM-5 catalyst at 50 °C (Fig. 4d). The observed peaks at 3646, 3372, and 1625 cm^{-1} can be assigned to the vibration of acidic OH species (Si-OH-Al), the adsorbed OH*, and H_2O* species, respectively [37,51]. The peaks at 1746 cm^{-1} and 1534 cm^{-1} can be assigned to the C=O vibration of the adsorbed CH_3COOH* species and the COO vibration of the adsorbed acetate molecule, [52] respectively. The identification of these intermediate compounds serves as additional evidence supporting the feasibility of directly converting CH_4 into CH_3COOH on the active Ni sites through the reaction with CO and H_2O_2 [24,25].

4. Conclusions

In summary, this work demonstrated that isolated nickel cations, anchored within the internal pores of zeolites, serve as the active species for the directly selective conversion of CH_4 into CH_3COOH via oxidative carbonylation. 2920 μmol/g$_{cat.}$ of oxygenated products can be acquired over the 1.2Ni-ZSM-5 catalyst, with a selectivity of up to 82.3 % for CH_3COOH. The catalytic performance of Ni-ZSM-5 for CH_3COOH production is comparable to these noble metal-based catalysts. Through isotopically labeled experiments and the monitoring of reaction intermediates, it can be determined that the formation of CH_3COOH originates directly from the coupling of CH_4 and CO, rather than through the involvement of intermediate products. This study provides a low-cost and well-designed Ni-based catalysts for oxidative CH_4 into high value-added C_{2+} oxygenates rather than traditional C_1 product.

CRediT authorship contribution statement

Yao Wei: Data curation, Formal analysis, Investigation, Writing – original draft. **Bo Wu:** Writing – original draft. **Jin Liu:** Writing – original draft. **Xuan Zhou:** Investigation. **Hailing Yu:** Writing – original draft. **Tiejun Lin:** Writing – review & editing. **Yuxin Liu:** Formal analysis, Investigation. **Ruitao Li:** Formal analysis, Investigation. **Liangshu Zhong:** Writing – review & editing.

Declaration of Competing Interest

The authors declare that they have no known competing financial interests or personal relationships that could have appeared to influence the work reported in this paper.

Data availability

Data will be made available on request.

Appendix A. Supporting information

Supplementary data associated with this article can be found in the online version at doi:10.1016/j.apcatb.2024.123951.

References

[1] J. Zhang, H. Meerman, R. Benders, A. Faaij, Potential role of natural gas infrastructure in China to supply low-carbon gases during 2020–2050, Appl. Energy 306 (2022) 117989.

[2] P. Kumar, T.A. Al-Attas, J. Hu, M.G. Kibria, Single atom catalysts for selective methane oxidation to oxygenates, ACS Nano 16 (2022) 8557–8618.

[3] Y. Tang, Y. Li, F. Tao, Activation and catalytic transformation of methane under mild conditions, Chem. Soc. Rev. 51 (2022) 376–423.

[4] L. Yang, H. Lin, Z. Fang, Y. Yang, X. Liu, G. Ouyang, Recent advances on methane partial oxidation toward oxygenates under mild conditions, Renew. Sustain. Energy Rev. 184 (2023) 113561.

[5] N.N. Ezhova, N.V. Kolesnichenko, A.L. Maximov, Modern methods for producing acetic acid from methane: new trends (A review), Pet. Chem. 62 (2022) 40–61.

[6] A. Caballero, P.J. Pérez, Methane as raw material in synthetic chemistry: the final frontier, Chem. Soc. Rev. 42 (2013) 8809–8820.

[7] R. Franz, E.A. Uslamin, E.A. Pidko, Challenges for the utilization of methane as a chemical feedstock, Mendeleev Commun. 31 (2021) 584–592.

[8] A.E. Shilov, G.B. Shul'pin, Activation of C-H bonds by metal complexes, Chem. Rev. 97 (1997) 2879–2932.

[9] S.J. Freakley, N. Dimitratos, D.J. Willock, S.H. Taylor, C.J. Kiely, G.J. Hutchings, methane oxidation to methanol in water, Acc. Chem. Res. 54 (2021) 2614–2623.

[10] C. Hammond, S. Conrad, I. Hermans, Oxidative methane upgrading, ChemSusChem 5 (2012) 1668–1686.

[11] R. Horn, R. Schlögl, Methane activation by heterogeneous catalysis, Catal. Lett. 145 (2014) 23–39.

[12] P. Tang, Q. Zhu, Z. Wu, D. Ma, Methane activation: the past and future, Energy Environ. Sci. 7 (2014) 2580–2591.

[13] A. Haynes, P.M. Maitlis, G.E. Morris, G.J. Sunley, H. Adams, P.W. Badger, C. M. Bowers, D.B. Cook, P.I. Elliott, T. Ghaffar, Promotion of iridium-catalyzed methanol carbonylation: Mechanistic studies of the cativa process, J. Am. Chem. Soc. 126 (2004) 2847–2861.

[14] P. Kalck, C. Le Berre, P. Serp, Recent advances in the methanol carbonylation reaction into acetic acid, Coord. Chem. Rev. 402 (2020) 213078.

[15] G.J. Sunley, D.J. Watson, High productivity methanol carbonylation catalysis using iridium: the Cativa™ process for the manufacture of acetic acid, Catal. Today 58 (2000) 293–307.

[16] M. Li, J. Shan, G. Giannakakis, M. Ouyang, S. Cao, S. Lee, L.F. Allard, M. Flytzani-Stephanopoulos, Single-step selective oxidation of methane to methanol in the aqueous phase on iridium-based catalysts, Appl. Catal. B: Environ. 292 (2021) 120124.

[17] M. Ravi, M. Ranocchiari, J.A. van Bokhoven, The direct catalytic oxidation of methane to methanol-a critical assessment, Angew. Chem. Int. Ed. 56 (2017) 16464–16483.

[18] M. Lin, A. Sen, Direct catalytic conversion of methane to acetic acid in an aqueous medium, Nature 368 (1994) 613–615.

[19] S. Chempath, A.T. Bell, Density functional theory analysis of the reaction pathway for methane oxidation to acetic acid catalyzed by Pd^{2+} in sulfuric acid, J. Am. Chem. Soc. 128 (2006) 4650–4657.

[20] T. Kitamura, Y. Ishida, T. Yamaji, Y. Fujiwara, A new catalytic system consisting of Mo for acetic acid synthesis from methane and CO, Bull. Chem. Soc. Jpn. 76 (2003) 1677–1678.

[21] J. Shan, M. Li, L.F. Allard, S. Lee, M. Flytzani-Stephanopoulos, Mild oxidation of methane to methanol or acetic acid on supported isolated rhodium catalysts, Nature 551 (2017) 605–608.

[22] Y. Tang, Y. Li, V. Fung, D.E. Jiang, W. Huang, S. Zhang, Y. Iwasawa, T. Sakata, L. Nguyen, X. Zhang, A.I. Frenkel, F. Tao, Single rhodium atoms anchored in micropores for efficient transformation of methane under mild conditions, Nat. Commun. 9 (2018) 1231.

[23] H. Li, C. Xiong, M. Fei, L. Ma, H. Zhang, X. Yan, P. Tieu, Y. Yuan, Y. Zhang, J. Nyakuchena, J. Huang, X. Pan, M.M. Waegele, D.E. Jiang, D. Wang, Selective formation of acetic acid and methanol by direct methane oxidation using rhodium single-atom catalysts, J. Am. Chem. Soc. 145 (2023) 11415–11419.

[24] C.W. Wang, Y. Sun, L.J. Wang, W.H. Feng, Y.T. Miao, M.M. Yu, Y.X. Wang, X. D. Gao, Q. Zhao, Z. Ding, Z. Feng, S.M. Yu, J. Yang, Y. Hu, J.F. Wu, Oxidative

carbonylation of methane to acetic acid on an Fe-modified ZSM-5 zeolite, Appl. Catal. B: Environ. 329 (2023) 122549.

[25] B. Wu, T. Lin, Z. Lu, X. Yu, M. Huang, R. Yang, C. Wang, C. Tian, J. Li, Y. Sun, L. Zhong, Fe binuclear sites convert methane to acetic acid with ultrahigh selectivity, Chem 8 (2022) 1658–1672.

[26] P. Kumar, P. Antal, X. Wang, J. Wang, D. Trivedi, O.F. Fellner, Y.A. Wu, I. Nemec, V.T. Santana, J. Kopp, Partial thermal condensation mediated synthesis of high-density nickel single atom sites on carbon nitride for selective photooxidation of methane into methanol, Small (2023) 2304574.

[27] F.F. Tao, J.J. Shan, L. Nguyen, Z. Wang, S. Zhang, L. Zhang, Z. Wu, W. Huang, S. Zeng, P. Hu, Understanding complete oxidation of methane on spinel oxides at a molecular level, Nat. Commun. 6 (2015) 7798.

[28] J. Shan, W. Huang, L. Nguyen, Y. Yu, S. Zhang, Y. Li, A.I. Frenkel, F. Tao, Conversion of methane to methanol with a bent mono (μ-oxo) dinickel anchored on the internal surfaces of micropores, Langmuir 30 (2014) 8558–8569.

[29] M.H. Mahyuddin, A. Staykov, Y. Shiota, K. Yoshizawa, Direct conversion of methane to methanol by metal-exchanged ZSM-5 zeolite (Metal = Fe, Co, Ni, Cu), ACS Catal. 6 (2016) 8321–8331.

[30] T. Moteki, N. Tominaga, M. Ogura, Mechanism investigation and product selectivity control on CO-assisted direct conversion of methane into C1 and C2 oxygenates catalyzed by zeolite-supported Rh, Appl. Catal. B: Environ. 300 (2022) 120742.

[31] B.R. Mitchell, Metal contamination of cracking catalysts. 1. Synthetic metals deposition on fresh catalysts, Ind. Eng. Chem. Prod. Res. Dev. 19 (1980) 209–213.

[32] M.A. Peck, M.A. Langell, Comparison of nanoscaled and bulk NiO structural and environmental characteristics by XRD, XAFS, and XPS, Chem. Mater. 24 (2012) 4483–4490.

[33] K.S. Sing, Reporting physisorption data for gas/solid systems with special reference to the determination of surface area and porosity (Recommendations 1984), Pure Appl. Chem. 57 (1985) 603–619.

[34] A.J. Maia, B. Louis, Y.L. Lam, M.M. Pereira, Ni-ZSM-5 catalysts: detailed characterization of metal sites for proper catalyst design, J. Catal. 269 (2010) 103–109.

[35] M.C. Biesinger, B.P. Payne, A.P. Grosvenor, L.W.M. Lau, A.R. Gerson, R.S.C. Smart, Resolving surface chemical states in XPS analysis of first row transition metals, oxides and hydroxides: Cr, Mn, Fe, Co and Ni, Appl. Surf. Sci. 257 (2011) 2717–2730.

[36] A.P. Grosvenor, M.C. Biesinger, R.S.C. Smart, N.S. McIntyre, New interpretations of XPS spectra of nickel metal and oxides, Surf. Sci. 600 (2006) 1771–1779.

[37] B.H. Chen, Z.S. Chao, H. He, C. Huang, Y.J. Liu, W.J. Yi, X.L. Wei, J.F. An, Towards a full understanding of the nature of Ni(II) species and hydroxyl groups over highly siliceous HZSM-5 zeolite supported nickel catalysts prepared by a deposition-precipitation method, Dalton Trans. 45 (2016) 2720–2739.

[38] I. Preda, R.J.O. Mossanek, M. Abbate, L. Alvarez, J. Méndez, A. Gutiérrez, L. Soriano, Surface contributions to the XPS spectra of nanostructured NiO deposited on HOPG, Surf. Sci. 606 (2012) 1426–1430.

[39] X. Li, B. Li, J. Xu, Synthesis and characterization of transitional metal-rich zeolite M-MFI (M = Fe, Co, Ni, Cu) with regular mesoporous channels, Colloids Surf. Physicochem. Eng. Asp. 434 (2013) 287–295.

[40] H.T. Vu, I. Arčon, D.O.D. Souza, S. Pollastri, G. Dražić, J. Volavšek, G. Mali, N. Zabukovec Logar, N. Novak Tušar, Insight into the interdependence of Ni and Al in bifunctional Ni/ZSM-5 catalysts at the nanoscale, Nanoscale Adv. 4 (2022) 2321–2331.

[41] X. Wang, S. Xi, P. Huang, Y. Du, H. Zhong, Q. Wang, A. Borgna, Y.W. Zhang, Z. Wang, H. Wang, Z.G. Yu, W.S.V. Lee, J. Xue, Pivotal role of reversible NiO_6 geometric conversion in oxygen evolution, Nature 611 (2022) 702–708.

[42] T. Ding, X. Liu, Z. Tao, T. Liu, T. Chen, W. Zhang, X. Shen, D. Liu, S. Wang, B. Pang, D. Wu, L. Cao, L. Wang, T. Liu, Y. Li, H. Sheng, M. Zhu, T. Yao, Atomically precise dinuclear site active toward electrocatalytic CO_2 reduction, J. Am. Chem. Soc. 143 (2021) 11317–11324.

[43] T. Kyômen, R. Yamazaki, M. Itoh, Valence and spin state of Co and Ni ions and their relation to metallicity and ferromagnetism in $LaCo_{0.5}Ni_{0.5}O_3$, Phys. Rev. B 68 (2003) 104416.

[44] G. Dublet, F. Juillot, G. Morin, E. Fritsch, V. Noel, J. Brest, G.E. Brown Jr, XAS evidence for Ni sequestration by siderite in a lateritic Ni-deposit from New Caledonia, Am. Mineral. 99 (2014) 225–234.

[45] C. Sun, K. Zhao, A. Boies, S. Xiao, Z. Yi, Boosting total oxidation of methane over NiO nanocrystalline decorated ZnO-CoNi solid solution via photothermal synergism, Appl. Catal. B: Environ. 339 (2023) 123124.

[46] G. Qi, T.E. Davies, A. Nasrallah, M.A. Sainna, A.G.R. Howe, R.J. Lewis, M. Quesne, C.R.A. Catlow, D.J. Willock, Q. He, D. Bethell, M.J. Howard, B.A. Murrer, B. Harrison, C.J. Kiely, X. Zhao, F. Deng, J. Xu, G.J. Hutchings, Au-ZSM-5 catalyses the selective oxidation of CH_4 to CH_3OH and CH_3COOH using O_2, Nat. Catal. 5 (2022) 45–54.

[47] M. Asadullah, T. Kitamura, Y. Fujiwara, Calcium-catalyzed selective and quantitative transformation of CH_4 and CO into acetic acid, Angew. Chem. Int. Ed. 39 (2000) 2475–2478.

[48] S. Bai, F. Liu, B. Huang, F. Li, H. Lin, T. Wu, M. Sun, J. Wu, Q. Shao, Y. Xu, High-efficiency direct methane conversion to oxygenates on a cerium dioxide nanowires supported rhodium single-atom catalyst, Nat. Commun. 11 (2020) 954.

[49] Q. Shen, C. Cao, R. Huang, L. Zhu, X. Zhou, Q. Zhang, L. Gu, W. Song, Single chromium atoms supported on titanium dioxide nanoparticles for synergic catalytic methane conversion under mild conditions, Angew. Chem. Int. Ed. 59 (2020) 1216–1219.

[50] M.H. Ab Rahim, M.M. Forde, R.L. Jenkins, C. Hammond, Q. He, N. Dimitratos, J. A. Lopez-Sanchez, A.F. Carley, S.H. Taylor, D.J. Willock, D.M. Murphy, C.J. Kiely, G.J. Hutchings, Oxidation of methane to methanol with hydrogen peroxide using supported aold-palladium alloy nanoparticles, Angew. Chem. Int. Ed. 52 (2013) 1280–1284.

[51] B.R. Wood, J.A. Reimer, A.T. Bell, M.T. Janicke, K.C. Ott, Methanol formation on Fe/Al-MFI via the oxidation of methane by nitrous oxide, J. Catal. 225 (2004) 300–306.

[52] W. Rachmady, M.A. Vannice, Acetic acid reduction by H_2 over supported Pt catalysts: A DRIFTS and TPD/TPR study,, J. Catal. 207 (2002) 317–330.